Compressed Sensing MRI Using Nonseparable Shearlet Transform and Split Bregman Algorithm

Venceslav Kafedziski and Slavche Pejoski

Abstract—We analyze the use of discrete nonseparable shearlet transform for sparse representation of the MRI image. This transform is a non-tight frame, but has excellent localization properties in the spatial domain. Additionally, we exploit the frequency representation of the canonical dual filters of this transform and combine it with the measurement process, carried out in the Fourier domain, to implement the split Bregman algorithm for reconstruction. We compare the performance of the proposed approach to approaches using split Bregman algorithm with curvelets, wavelets and total variation.

Index Terms—MRI, compressed sensing, split Bregman algorithm, discrete nonseparable shearlet transform (DNST)

I. Introduction

IN magnetic resonance imaging (MRI) [1], due to hardware and physiological constraints, the scanning time is crucial [2]. It can be reduced by using compressed sensing (CS) [3]. CS allows for good quality of the MRI reconstructed image when reduced number of samples are acquired during the MRI scanning process. The quality of the reconstructed image in CS depends on the measurement process, the sparsifying transform and the reconstruction algorithm. We propose the use of the discrete nonseparable shearlet transform (DNST) [4], [5] as a sparsifying transform and implement the split Bregman iterative algorithm [6]–[8] for reconstruction. The choice of the DNST is due to its good localization capabilities in the spatial domain and improved directional selectivity [4]. However, since it is not a tight frame, the simple analysis based reconstruction algorithms constructed for tight frames [7] cannot be directly applied without sacrificing some performance. Possible solutions for non-tight frames are the combination of split Bregman algorithm and conjugate gradient step [8], which is complex and slow, and the proximity approach proposed in [9], [10], which is a synthesis based approach. One very useful feature of DNST is that its canonical dual synthesis filters are related to its analysis filters in the Fourier domain by simple scaling relations, where the scaling factors are equal for all the synthesis filters. This provides a fast implementation of the synthesis and analysis operations, which combined with the MRI measurement process, carried out in the Fourier domain, allows for simple implementation of the split Bregman algorithm. The contribution of this paper comes from the implementation of the split Bregman reconstruction algorithm adapted to the features of the DNST and the MRI, and the estimation of the performance gain compared to the case when the algorithm is implemented assuming that the transform is a tight frame.

V. Kafedziski and S. Pejoski are with the Faculty of Electrical Engineering and Information Technologies, University Ss Cyril and Methodius, Skopje, Republic of Macedonia (e-mail: kafedzi@feit.ukim.edu.mk, slavchep@feit.ukim.edu.mk).

The rest of the paper is organized as follows. In the second section we explain the basics of MRI, CS, discrete nonseparable shearlet transform and split Bregman algorithm. In the third section we explain the implementation of the reconstruction algorithm. In section IV we present the simulation results where we compare the performance of DNST split Bregman compressed sensing MRI (for both implementations: the matched to DNST, and the implementation assuming that the DNST is a tight frame) with compressed sensing MRI using the split Bregman algorithm with different sparsifying transforms or regularization: wavelet, curvelet and total variation (TV) for different sampling patterns and for different MRI images. Section V concludes the paper.

II. Description of the System

A. MRI basics

Since we deal with MRI images, we introduce notation for 2D signals in the spatial domain and in the 2D DFT domain. We assume that the image is represented by an $N \times N$ matrix $\mathbf{X}$. During the MRI sampling process, at each sampling instance, a single point in the so called k-space is obtained. The k-space is the 2D Fourier transform of the image, that represents the spatial distribution of the transverse magnetization in a thin slice of the body. The position of the sampled points in the k-space are controlled by specifically designed electromagnetic pulses and gradient fields [2]. To speed up the sampling process, in the compressed sensing approaches, some of the points in the k-space are omitted, leading to undersampling. The usual way to undersample the k-space is by randomly choosing vertical or horizontal sampling lines, using radial lines or variable density spirals [2]. Despite its impracticality, random variable density undersampling is also studied [2], [11]. Denoting the 2D DFT transform operator as $\mathcal{F}$ and the point sampling operator as $\mathbf{P}$, the sampling process can be described as $\mathbf{Y} = \mathbf{P}\mathcal{F}\mathbf{X} = \mathbf{M} \odot \hat{\mathbf{X}}$, where $\hat{\mathbf{X}} = \mathcal{F}\mathbf{X}$ is $N \times N$ matrix representing the 2D DFT of the image $\mathbf{X}$, $\odot$ is an element wise multiplication, $\mathbf{M}$ is an $N \times N$ matrix associated with the sampling operator $\mathbf{P}$ and $\mathbf{Y}$ is an $N \times N$ matrix representing the sampled 2D DFT. $\mathbf{M}$ has values equal to 1 in the positions where the k-space is sampled, and 0's elsewhere. The adjoint operator $\mathbf{P}^*$ of operator $\mathbf{P}$ is also element wise multiplication with $\mathbf{M}$.

B. Compressed sensing basics

We assume that the image $\mathbf{X}$ is undersampled during the measurement process, resulting in $\mathbf{Y} = \mathbf{\Phi}\mathbf{X}$. We assume that there exists a sparse representation $\mathbf{s}$ of that image in some sparsifying domain, $\mathbf{X} = \mathbf{\Psi}^*\mathbf{s}$, where $\mathbf{s}$ is the $L \times 1$ vector of transform coefficients. Then, the theory of compressed sensing [3], provides the conditions for perfect reconstruction of $\mathbf{X}$

from $\mathbf{Y}$. The most commonly used reconstruction approach is the minimization of the ℓ_1-norm:

$$\min_{\mathbf{s}} ||\mathbf{s}||_1 \quad \text{s.t.} \quad \mathbf{Y} = \mathbf{\Phi\Psi}^*\mathbf{s} \tag{1}$$

where $||\mathbf{s}||_1 = \sum_{l=1}^{L} |s(l)|$ represents the vector ℓ_1-norm. For the considered MRI system $\mathbf{\Phi} = \mathbf{P\mathcal{F}}$. In the ordinary CS setting [3] $\mathbf{\Psi}$ is the analysis operator associated with the sparsifying orthonormal basis, resulting in the transform coefficients $\mathbf{s} = \mathbf{\Psi X}$, $\mathbf{\Psi}^*$ is the synthesis (adjoint) operator associated with $\mathbf{\Psi}$, so that $\mathbf{\Psi}^*\mathbf{\Psi X} = \mathbf{X}$.

The most commonly used condition on the $\mathbf{\Phi\Psi}^*$ that guarantees perfect reconstruction is the Restricted Isometry Property (RIP), which was originally derived for orthogonal sparsifying transforms. Recently, it has been extended to the case when the sparsifying transform is an arbitrary frame operator [8]. As explained in [8] there are infinitely many dual frames for a given frame, but here we use the canonical dual frame. We denote the frame operator and its adjoint as $\mathbf{\Psi}_b$ and $\mathbf{\Psi}_b^*$ and the dual frame and its adjoint as $\mathbf{\Psi}_c$ and $\mathbf{\Psi}_c^*$. Then, the reconstruction can be obtained as $\mathbf{\Psi}_b^*\mathbf{\Psi}_c\mathbf{X} = \mathbf{X}$ or $\mathbf{\Psi}_c^*\mathbf{\Psi}_b\mathbf{X} = \mathbf{X}$.

When $\mathbf{X}$ is not sparse but is compressible in some domain, or is contaminated with an additive noise, (1) is changed to:

$$\min_{\mathbf{s}} \lambda||\mathbf{s}||_1 + \frac{1}{2}||\mathbf{Y} - \mathbf{\Phi\Psi}_c^*\mathbf{s}||_F^2 \tag{2}$$

In (2), $||\mathbf{X}||_F = \sqrt{\sum_{m=1}^{N}\sum_{n=1}^{N} |X(m,n)|^2}$ is the Frobenius matrix norm and λ depends on the compressibility of the image and the noise level.

C. Discrete nonseparable shearlet transform (DNST) basics

To improve the capabilities of classical wavelet transforms for sparse representation of functions with spatially distributed discontinuities, the shearlet transform has three operators: dilation, translation and shearing operator [12]. For the 2D case, the shearing operator is based on the shearing matrix $S_k = \begin{pmatrix} 1 & k \\ 0 & 1 \end{pmatrix}$, where $k \in \mathbb{Z}$, the dilation operator is based on the parabolic scaling matrices $A_{2^j} = \begin{pmatrix} 2^j & 0 \\ 0 & 2^{\lfloor j/2 \rfloor} \end{pmatrix}$, where $j \geq 0$, and the translation operation is defined in terms of $c = (c_1, c_2) \in (\mathbb{R}_+)^2$. 2D discrete shearlet transform is usually obtained using a cone adapted shearlet system, defined by scaling and shearlet functions ϕ_m, $\psi_{j,k,m}$ and $\tilde{\psi}_{j,k,m}$, generated by the scaling generator $\phi \in L^2(\mathbb{R}^2)$, parameterized by translation parameter m, and the shearlet generators $\psi \in L^2(\mathbb{R}^2)$ and $\tilde{\psi} \in L^2(\mathbb{R}^2)$, parameterized by the scaling parameter j, translation parameter m and shear parameter k. Note that $\tilde{\psi}_{j,k,m}$ are obtained from $\psi_{j,k,m}$ by swapping the two variables.

For DNST, ψ is constructed from a separable compactly supported shearlet generator (leads to excellent localization properties), and a 2D nonseparable fan filter (for improved directional selectivity). For the details about the discretization of all the functions included in the DNST system in order to obtain the digital shearlet filters $\phi^d, \psi_{j,k}^d, \tilde{\psi}_{j,k}^d \in l^2(\mathbb{Z}^2)$, we refer the interested reader to [4], [5]. For the special choice of $c_1 = 2^{j-J}$ and $c_2 = 2^{j/2-J}$, where J is the number of values of the scaling parameter j ($0 \leq j \leq J - 1$), the DNST is

obtained by a series of filtering operations (2D convolutions) of the image with $\overline{\phi^d}$, $\overline{\psi^d}_{j,k}$ and $\overline{\tilde{\psi}^d}_{j,k}$, where $\overline{z}(\mathbf{n}) = z(-\mathbf{n})$, $\mathbf{n} \in \mathbb{Z}^2$. This corresponds to an element wise multiplication in the 2D DFT domain. Additionally, the 2D DFT's of the canonical dual shearlet filters can be evaluated from the 2D DFT's of the shearlet filters $\hat{\phi}^d = \mathcal{F}(\phi^d)$, $\hat{\psi}_{j,k}^d = \mathcal{F}(\psi_{j,k}^d)$, $\hat{\tilde{\psi}}_{j,k}^d = \mathcal{F}(\tilde{\psi}_{j,k}^d)$:

$$\hat{h}^d(w1, w2) = \frac{\hat{\phi}^d(w_1, w_2)}{\hat{\Gamma}(w_1, w_2)}$$

$$\hat{\gamma}_{j,k}^d(w1, w2) = \frac{\hat{\psi}_{j,k}^d(w_1, w_2)}{\hat{\Gamma}(w_1, w_2)}$$

$$\hat{\tilde{\gamma}}_{j,k}^d(w1, w2) = \frac{\hat{\tilde{\psi}}_{j,k}^d(w_1, w_2)}{\hat{\Gamma}(w_1, w_2)}$$

$$\hat{\Gamma}(w_1, w_2) = |\hat{\phi}^d(w_1, w_2)|^2$$
$$+ \sum_{j=0}^{J-1} \sum_{|k| \leq 2^{\lceil j/2 \rceil}} (|\hat{\psi}_{j,k}^d(w_1, w_2)|^2$$
$$+ |\hat{\tilde{\psi}}_{j,k}^d(w_1, w_2)|^2) \tag{3}$$

In (3) the value of $\hat{\Gamma}(w_1, w_2)$ doesn't depend on the scale or the shear, and has the same value for all dual filters. The reconstruction formula is given by:

$$\mathbf{X} = (\mathbf{X} * \overline{\phi^d}) * h^d + \sum_{j=0}^{J-1} \sum_{|k| \leq 2^{\lceil j/2 \rceil}} (\mathbf{X} * \overline{\psi^d}_{j,k}) * \gamma_{j,k}^d$$
$$+ \sum_{j=0}^{J-1} \sum_{|k| \leq 2^{\lceil j/2 \rceil}} (\mathbf{X} * \overline{\tilde{\psi}^d}_{j,k}) * \tilde{\gamma}_{j,k}^d \tag{4}$$

The transform coefficients of the image $\mathbf{X}$ can be obtained as $\mathbf{s} = \mathbf{\Psi}_b\mathbf{X}$, where $\mathbf{\Psi}_b$ corresponds to the application of the 2D shearlet filters, associated with DNST. Similarly, the reconstruction (4) can be written as $\mathbf{X} = \mathbf{\Psi}_c^*\mathbf{s} = \mathbf{\Psi}_c^*\mathbf{\Psi}_b\mathbf{X}$, where $\mathbf{\Psi}_c^*$ is associated with the application of the dual shearlet filters in the reconstruction formula (4) to the transform coefficients. Due to the form of $\hat{\Gamma}(w_1, w_2)$, the DNST has the following property $\mathcal{F}(\mathbf{\Psi}_b^*\mathbf{\Psi}_b\mathbf{X}) = \hat{\Gamma} \odot \mathcal{F}(\mathbf{X})$, which will be used in the split Bregman algorithm. Namely, the reconstruction $\mathbf{G} = \mathbf{\Psi}_b^*\mathbf{\Psi}_b\mathbf{X}$ is based on the application of the filters associated with the original frame, which in the 2D DFT domain obtains the following form:

$$\hat{\mathbf{G}}(w_1, w_2) = (\hat{\mathbf{X}}(w_1, w_2)\hat{\phi}^d(w_1, w_2)^*)\hat{\phi}^d(w_1, w_2)$$
$$+ \sum_{j=0}^{J-1} \sum_{|k| \leq 2^{\lceil j/2 \rceil}} (\hat{\mathbf{X}}(w_1, w_2)\hat{\psi}_{j,k}^d(w_1, w_2)^*)\hat{\psi}_{j,k}^d(w_1, w_2)$$
$$+ \sum_{j=0}^{J-1} \sum_{|k| \leq 2^{\lceil j/2 \rceil}} (\hat{\mathbf{X}}(w_1, w_2)\hat{\tilde{\psi}}_{j,k}^d(w_1, w_2)^*)\hat{\tilde{\psi}}_{j,k}^d(w_1, w_2) =$$
$$= \hat{\Gamma}(w_1, w_2)\hat{\mathbf{X}}(w_1, w_2) \tag{5}$$

D. The split Bregman algorithm

The analysis form of (2), suitable for the application of the split Bregman algorithm is:

$$\min_{\mathbf{X}} \lambda||\mathbf{\Psi}_b\mathbf{X}||_1 + \frac{1}{2}||\mathbf{Y} - \mathbf{\Phi X}||_F^2 \tag{6}$$

The split Bregman method finds the solution of the problem (6) by introducing the new variable $\mathbf{u} = \mathbf{\Psi}_b\mathbf{X}$, which leads to the following Bregman iterations:

$$(\mathbf{X}^{k+1}, \mathbf{u}^{k+1}) = \min_{\mathbf{X}, \mathbf{u}} \lambda ||\mathbf{u}||_1 + \frac{1}{2}||\mathbf{Y} - \mathbf{\Phi X}||_F^2$$
$$+ \frac{\mu}{2}||\mathbf{u} - \mathbf{\Psi}_b \mathbf{X} - \mathbf{b}_c^k||_2^2$$
$$\mathbf{b}_c^{k+1} = \mathbf{b}_c^k + \mathbf{\Psi}_b \mathbf{X}^{k+1} - \mathbf{u}^{k+1} \qquad (7)$$

where $||\mathbf{s}||_2^2 = \sum_{l=1}^{L} |s(l)|^2$ and μ is a constant associated with the algorithm [6], [7]. The complete procedure of obtaining the split Bregman iteration in (7) from (6) is described in [6]–[8] together with the analysis of the convergence properties of the algorithm. The authors of those papers propose a procedure for solving the minimization in (7), where the minimization is separately solved for the two different variables in an iterative manner. The split Bregman iterations now become:

$$\mathbf{X}^{k+1} = \min_{\mathbf{X}} \frac{1}{2}||\mathbf{Y} - \mathbf{\Phi X}||_F^2$$
$$+ \frac{\mu}{2}||\mathbf{u}^k - \mathbf{\Psi}_b \mathbf{X} - \mathbf{b}_c^k||_2^2$$
$$\mathbf{u}^{k+1} = \min_{\mathbf{u}} \lambda ||\mathbf{u}||_1 + \frac{\mu}{2}||\mathbf{u} - \mathbf{\Psi}_b \mathbf{X}^{k+1} - \mathbf{b}_c^k||_2^2$$
$$\mathbf{b}_c^{k+1} = \mathbf{b}_c^k + \mathbf{\Psi}_b \mathbf{X}^{k+1} - \mathbf{u}^{k+1} \qquad (8)$$

The second minimization in (8) is easily solved by applying soft thresholding to the components of $\mathbf{e} = \mathbf{\Psi}_b \mathbf{X}^{k+1} + \mathbf{b}_c^k$ with a thresholding level λ/μ i.e. $\mathbf{u}^{k+1} = \mathcal{T}_{\lambda/\mu}(\mathbf{e})$, defined as:

$$u^{k+1}(l) = \begin{cases} \text{sign}(e(l)) \cdot (|e(l)| - \lambda/\mu) & |e(l)| > \lambda/\mu \\ 0 & |e(l)| \leq \lambda/\mu, \end{cases} \qquad (9)$$

where $\text{sign}(\cdot)$ is the sign function and $l = 1, ..., L$. In the following section we present a procedure for the explicit solution of the first minimization of (8).

III. IMPLEMENTATION OF THE RECONSTRUCTION ALGORITHM

The first minimization in (8) can be solved by finding its derivative and setting it to $\mathbf{0}$. Using the properties of linear operators we get:

$$\mathbf{\Phi}^* \mathbf{\Phi X} + \mu \mathbf{\Psi}_b^* \mathbf{\Psi}_b \mathbf{X} = \mathbf{\Phi}^* \mathbf{Y} + \mu \mathbf{\Psi}_b^* (\mathbf{u}^k - \mathbf{b}_c^k) \qquad (10)$$

Noticing that $\mathbf{\Phi}^* \mathbf{Y} = \mathcal{F}^* \mathbf{P}^* \mathbf{Y} = \mathcal{F}^*(\mathbf{M} \odot \mathbf{Y})$, using the substitutions $\mathbf{u}^k = \mathbf{\Psi}_b \tilde{\mathbf{U}}^k$, $\mathbf{b}_c^k = \mathbf{\Psi}_b \tilde{\mathbf{B}}_c^k$, $\hat{\tilde{\mathbf{U}}}^k = \mathcal{F} \tilde{\mathbf{U}}^k$ and $\hat{\tilde{\mathbf{B}}}_c^k = \mathcal{F} \tilde{\mathbf{B}}_c^k$, and applying 2D DFT to both sides of (10), we obtain the following 2D equation:

$$\mathbf{M} \odot \hat{\mathbf{X}} + \mu \hat{\Gamma} \odot \hat{\mathbf{X}} = \mathbf{M} \odot \mathbf{Y} + \mu \hat{\Gamma} \odot (\hat{\tilde{\mathbf{U}}}^k - \hat{\tilde{\mathbf{B}}}_c^k) \qquad (11)$$

Since the components of $\hat{\mathbf{X}}$ in (11) are decoupled, they can be explicitly solved for, as shown in (12) at the bottom of this page. Similar DFT form solution of the first minimization in (8) can be found in [13], but, in that work, the algorithm adapts to the features of the TV regularization parameter, while we use DNST.

The matrix $\mathbf{X}^{k+1}$ is obtained by applying an inverse 2D DFT to the matrix $\hat{\mathbf{X}}$ from (12). Since all the elements of $\mathbf{X}^{k+1}$ are positive real numbers, an additional operation of keeping the real parts and truncating to nonnegative values of the elements of $\mathbf{X}^{k+1}$ can be carried out for each iteration. This improves the reconstructed image quality [14], and, thus, we use it in the algorithm.

(a) Image 1   (b) Image 2
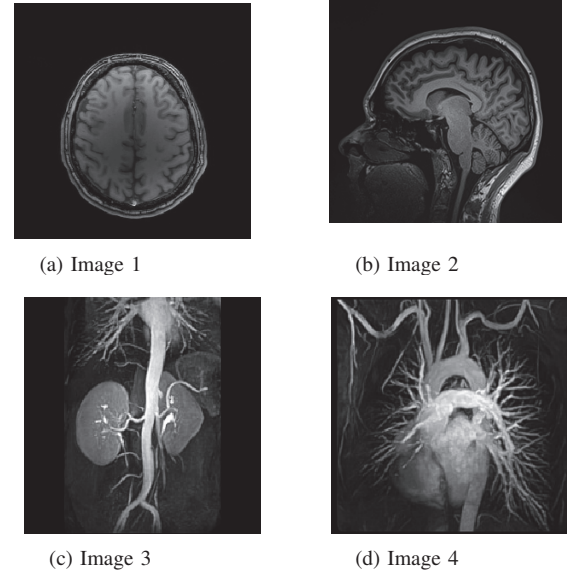
(c) Image 3   (d) Image 4

Fig. 1. The images used for testing the performance of the algorithm

To avoid keeping the values of both $\tilde{\mathbf{U}}^k$, $\tilde{\mathbf{B}}_c^k$, and $\mathbf{u}^k$ and $\mathbf{b}_c^k$, we substitute the second and the third equation in (8) with:

$$\tilde{\mathbf{U}}^{k+1} = \mathbf{\Psi}_c^* \mathcal{T}_{\lambda/\mu}(\mathbf{\Psi}_b(\mathbf{X}^{k+1} + \tilde{\mathbf{B}}_c^k)) \qquad (13)$$
$$\tilde{\mathbf{B}}_c^{k+1} = \tilde{\mathbf{B}}_c^k + \mathbf{X}^{k+1} - \tilde{\mathbf{U}}^{k+1}$$

When $\mathbf{\Psi}_b$ is a Parseval frame, $\hat{\Gamma}(w_1, w_2) = 1$, and our algorithm becomes the alternating split Bregman algorithm in spatial domain ([7], table 2) for a single tight frame with calculation of the first minimization in (8) using the 2D DFT.

In (12), for very low values of μ, $\hat{\mathbf{X}}^{k+1}$ will be almost independent of $\hat{\Gamma}(w_1, w_2)$. This is important when the values of $\hat{\Gamma}(w_1, w_2)$ are unknown or hard to calculate. If we start the algorithm with a small value of μ, the dominant part will be $\mathbf{Y}(w_1, w_2)$ and the algorithm will have a good start. As the value of μ increases, the difference between the quality of the reconstructed image when using the true values $\hat{\Gamma}(w_1, w_2)$ and $\hat{\Gamma}(w_1, w_2) = 1$ (the tight frame assumption) increases, but remains small.

IV. SIMULATION

In order to evaluate the performance of the implemented algorithm we used four images of different human body parts or different views of them. The images are shown in Figure 1. The images 3 and 4 were taken from the publicly available software accompanying [14] and the first two images were obtained form a fully sampled MRI scan.

For comparison we used the split Bregman algorithm from [7] in a single transform setting, where we used an orthonormal wavelet transform (Daubechies length 4 filter with 4 scales) and curvelets [15]. We also used a split Bregman algorithm for TV based reconstruction where the first step of each Bregman iteration was taken from [13]. In the TV based algorithm we used the isotropic setting since it showed better performance. Additionally, we used an adapted to DNST version of the algorithm in [7], by solving the first minimization in (8) assuming that the DNST was a tight frame. In

$$\hat{\mathbf{X}}(w_1, w_2) = \begin{cases} \frac{\mathbf{Y}(w_1, w_2) + \mu \hat{\Gamma}(w_1, w_2)(\hat{\tilde{\mathbf{U}}}^k(w_1, w_2) - \hat{\tilde{\mathbf{B}}}_c^k(w_1, w_2))}{1 + \mu \hat{\Gamma}(w_1, w_2)} & \mathbf{M}(w_1, w_2) = 1 \\ \hat{\tilde{\mathbf{U}}}^k(w_1, w_2) - \hat{\tilde{\mathbf{B}}}_c^k(w_1, w_2) & \mathbf{M}(w_1, w_2) = 0 \end{cases} \qquad (12)$$

(a) Random sampling (sampling ratio: 20%)

(b) Radial lines (sampling ratio: 18.7%)

(c) Random horizontal lines (sampling ratio: 18%)

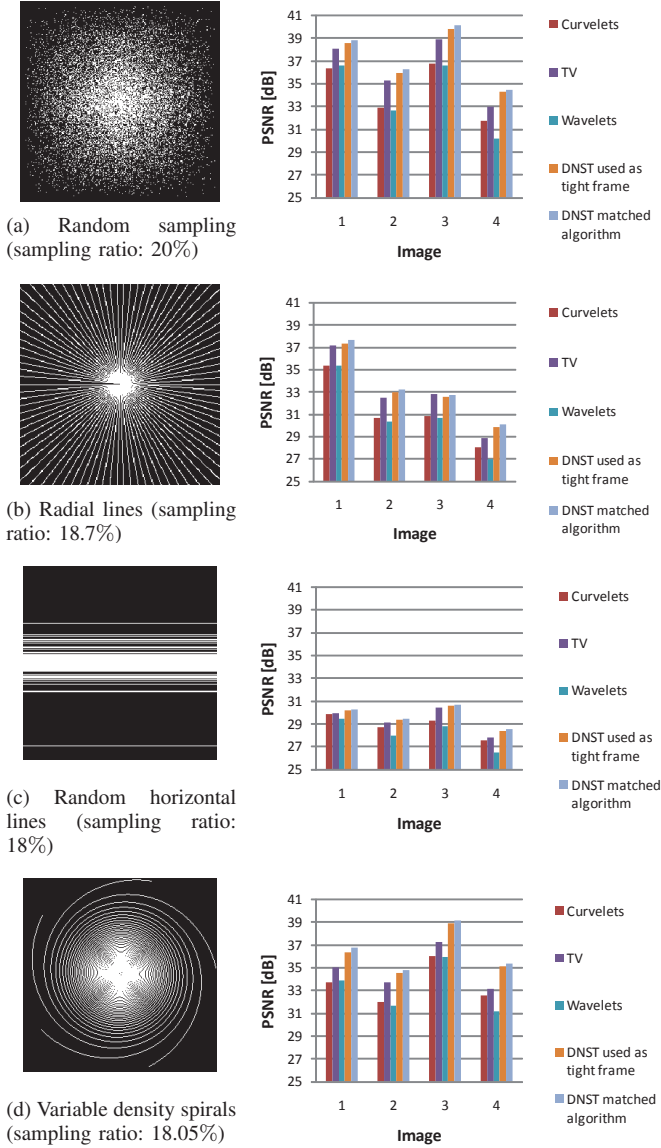(d) Variable density spirals (sampling ratio: 18.05%)

Fig. 2. The sampling patterns and the PSNR performance of different reconstruction algorithms for images from figure 1.

all the experiments we used increasing values of μ according to $\mu = 0.2(1 + i/N_{iter})$ where i was the order of iteration and N_{iter} was the total number of iterations (set to 50 for all the experiments). The noise in the system was set to 0. For each of the algorithms where DNST wasn't used and for each image, we searched for the value of λ on the grid $\mathbf{\Lambda} = 10^{-3}[2^{-3}, 2^{-2}, 2^{-1}, 1, 2, 4, 8]$ resulting in the highest obtained PSNR. In order to obtain similar grid behavior, when we used the DNST based algorithms based, we set the grid to $\mathbf{\Lambda}/5$. We used the four most commonly used sampling patterns: the random variable density undersampling, random horizontal lines, radial lines approximated with Cartesian points and variable density spiral trajectories approximated with Cartesian points. For the DNST we used the ShearLab 3D software [16] with 4, 4, 8 and 8 digital shearlet filters for scales $j = 0, 1, 2, 3$ respectively ($J = 4$).

The performance of the different algorithms for all the undersampling patterns and images is shown in Figure 2. From Figure 2, the implemented algorithm using DNST shows best performance for almost all sampling patterns and images. The performance gain is the most signficant for the random

undersampling, where the average gain is 3.4 dB compared to using wavelet transform, 3 dB compared to using curvelets, 1.1 dB compared to using TV and 0.3 dB compared to the case when using DNST in the tight frame algorithm version. These average gains drop to 1.5 dB, 0.87 dB, 0.4 dB and 0.1 dB for the random horizontal lines undersampling. The gain compared to the case when utilizing DNST in the tight frame algorithm version is small (the highest average value is for the random undersampling and it is equal to 0.3 dB), but always exists. This average gain can be observed as a rough estimate of the gain obtained by the proposed implementation of the split Bregman algorithm, in addition to the gain obtained by using the DNST.

V. CONCLUSION

We analyzed the use of the DNST as a sparsifying transform for compressed sensing MRI and implemented a fast split Bregman reconstruction algorithm matched to the DNST. The use of DNST resulted in an improved PSNR ranging from 0.4 dB to 3.4 dB compared to the use of curvelets, wavelets and TV with different sampling patterns. The contribution of the matched implementation of the split Bregman algorithm compared to the implementation that treats the DNST as a tight frame ranged from 0.1 dB to 0.3 dB.

REFERENCES

[1] G. Wright, "Magnetic resonance imaging," *IEEE Signal Processing Magazine*, vol. 14, no. 1, pp. 56 –66, jan 1997.

[2] M. Lustig, D. Donoho, and J. M. Pauly, "Sparse MRI: The application of compressed sensing for rapid MR imaging." *Magnetic resonance in medicine*, vol. 58, no. 6, pp. 1182–1195, 2007.

[3] D. L. Donoho, "Compressed sensing," *IEEE Transactions on Information Theory*, vol. 52, no. 4, pp. 1289–1306, 2006.

[4] W.-Q. Lim, "Nonseparable shearlet transform," *IEEE Transactions on Image Processing*, vol. 22, no. 5, pp. 2056–2065, 2013.

[5] G. Kutyniok, W.-Q. Lim, and X. Zhuang, "Digital shearlet transforms," in *Shearlets*, ser. Applied and Numerical Harmonic Analysis, G. Kutyniok and D. Labate, Eds. Birkhuser Boston, 2012, pp. 239–282.

[6] T. Goldstein and S. Osher, "The split Bregman method for L1-regularized problems," *SIAM Journal of Imaging Sciences*, vol. 2, no. 2, pp. 323–343, 2009.

[7] G. Plonka and J. Ma, "Curvelet-wavelet regularized split Bregman iteration for compressed sensing," *IJWMIP*, vol. 9, no. 1, pp. 79–110, 2011.

[8] Y. Liu, T. Mi, and S. Li, "Compressed sensing with general frames via optimal-dual-based ℓ_1 -analysis," *IEEE Transactions on Information Theory*, vol. 58, no. 7, pp. 4201–4214, 2012.

[9] C. Chaux, P. L. Combettes, J.-C. Pesquet, and V. R. Wajs, "A variational formulation for frame-based inverse problems," *Inverse Problems*, pp. 1495–1518, 2007.

[10] A. Beck and M. Teboulle, "A fast iterative shrinkage-thresholding algorithm for linear inverse problems," *SIAM Journal of Imaging Science*, vol. 2, no. 1, pp. 183–202, 2009.

[11] S. Pejoski and V. Kafedziski, "Wavelet image decomposition based variable density compressive sampling in mri," in *Proceedings of 19th Telecommunications Forum (TELFOR)*, 2011, pp. 635–638.

[12] G. Kutyniok and D. Labate, "Introduction to shearlets," in *Shearlets*, ser. Applied and Numerical Harmonic Analysis, G. Kutyniok and D. Labate, Eds. Birkhuser Boston, 2012, pp. 1–38.

[13] J. Yang, Y. Zhang, and W. Yin, "A fast alternating direction method for TVL1-L2 signal reconstruction from partial Fourier data," *IEEE Journal of Selected Topics in Signal Processing*, vol. 4, no. 2, pp. 288–297, 2010.

[14] J. Huang, S. Zhang, and D. Metaxas, "Efficient MR image reconstruction for compressed MR imaging," *Medical Image Analysis*, vol. 15, no. 5, pp. 670 – 679, 2011.

[15] E. Candés, L. Demanet, D. Donoho, and L. Ying, "Fast discrete curvelet transforms," *Multiscale Modeling & Simulation*, vol. 5, no. 3, pp. 861–899, 2006.

[16] "ShearLab 3D software, http://www.shearlab.org/index_software.html."